High performance of superconducting $YBa_2Cu_3O_7$ thick films prepared by single deposition inkjet-printing

Bohores Villarejo[†], Flavio Pino[†], Cornelia Pop[†], Susagna Ricart[†], Ferran Vallès[†], Bernat Mundet[†], Anna Palau[†], Pere Roura-Grabulosa[††], Jordi Farjas[††], Natalia Chamorro[†††], Ramón Yáñez[†††], Xavier Granados[†], Teresa Puig[†,*] Xavier Obradors[†,*]

[†] Institut de Ciència de Materials de Barcelona, ICMAB-CSIC, Campus de la UAB, 08193 Bellaterra, Catalonia, Spain

[††] University of Girona, Montilivi Campus, Edif. PII, 17071 Girona, Catalonia, Spain

[†††] Dpt Química, Universitat Autònoma de Barcelona, 08193 Bellaterra, Catalonia, Spain

ABSTRACT: Inkjet-printing is a very appealing cost-effective deposition technique to achieve large area solution derived functional films. For many applications it is very challenging to increase the film thickness in order to achieve competitive performance, for instance, high critical currents in superconducting films. In this paper, the preparation of superconducting $YBa_2Cu_3O_7$ thick films (~ 1.1 μm) using a single deposition is reported. Specific rules for ink design, deposition protocols and pyrolysis process are provided. The most important aspect is to formulate an ink with a solvent having a low evaporation rate that keeps the whole film wet during deposition to avoid liquid movement due to coffee-ring effects. An additional success has been to modify the ink with a photocurable polyacrylic ester varnish which after polymerization with a UV LED lamp helps to keep homogeneous thickness. This varnish also helped to avoid the generation of film instabilities (wrinkling or cracking) during pyrolysis. Homogeneous pyrolyzed thick films are transformed into epitaxial thick films with high critical currents. The inkjet-printing process is shown to be valid to prepare nanocomposite films using colloidal inks including pre-prepared $BaZrO_3$ nanoparticles. The nanocomposite thick films display enhanced vortex pinning thus keeping high critical currents under high magnetic fields.

INTRODUCTION

Achieving large film thicknesses is a key objective in many functional materials because their performance is greatly magnified. This objective has been widely pursued in all film deposition and growth methodologies with diverse degree of success. It is a particular materials processing hurdle for Chemical Solution Deposition (CSD). This is an appealing route for large area and low cost functional films which has been widely investigated to prepare inorganic or organic ferroelectric, piezoelectric, magnetic, semiconducting, optical or superconducting films [1–8].

Additional attractive features of CSD are a strong flexibility in defining composition, creating multilayer architectures and its suitability to generate nanocomposite structures through complex or colloidal solutions [9–22]. In recent years, extensive knowledge about epitaxial growth of CSD-based films has been generated in the context of improving their performances [4,23–26]. Growth of high temperature superconducting (HTS) cuprate epitaxial thin films by CSD has been widely investigated due to their strong potential as conductors for electrical power (cables, rotating machinery, fault current limiters) and magnet applications [27–30]. Epitaxial growth is achieved using either single crystalline or biaxially textured buffered metallic substrates, i.e. a so-called coated conductor architecture is generated [27,29]. To achieve high conductor performances, the film needs to be as thick as possible because the critical current for unit width I_c (the maximum current to be transported without dissipation) of a conductor increases linearly with the film thickness, i.e. $I_c = J_c \times t$, where t is the film thickness and J_c is the critical current density[27].

Up to now, the CSD approaches achieve, in a single deposition, thicknesses in the range of a few to some hundreds nm [4,31–33]. Most of power HTS applications require, however, thicker films, in the range of at least one micrometer. As a consequence, CSD of YBCO relies on multideposition processes where repetitive ink deposition – pyrolysis (organic matter decomposition at low temperatures) cycles are performed. This is a quite cum-

bersome process limiting its industrial attractiveness, and additionally, it leads to interfacial phase separation (interlayers) which compromise the final quality of the films [24,31,32,34]. For all those reasons, it is very challenging to develop a process allowing to increase the film thickness in a single CSD deposition. For this purpose, the use of the thorough understanding of the physicochemical transformations associated to the deposition and pyrolysis steps needs to be carefully considered [35–40].

When films with large areas or long lengths are required, as in the case of HTS coated conductors (CCs) based on $YBa_2Cu_3O_7$ (YBCO), an adapted deposition technique is required, i.e. the classical laboratory scale spin coating deposition process is not suitable. Ink Jet Printing (IJP) is a deposition methodology with a high potential to comply with the large scale requirements, as well as for the needs of patterned films, combinatorial and high throughput experimentation approaches. [41–43] IJP of YBCO thin films has been already demonstrated [44–46] and some knowledge has been generated concerning ink design, definition of the deposition conditions on specific substrates, the solution drying process, the pyrolysis step and the final epitaxial growth [20,45]. However, very little efforts have been reported up to now to use IJP for thick films preparation (in the range of 1 µm) using a single deposition [31].

Two sort of difficulties have limited the progress towards this goal. First, liquid movement during deposition or drying, due to coffee ring effects, usually leads to inhomogeneous thicknesses that degrade film performances [47–50]. Second, during the pyrolysis step, film shrinkage results in in-plane elastic stress which is strongly amplified when the film gets thicker. For this reason, thick CSD films have a strong tendency to form cracks and wrinkled structures degrading their performances [1,36,51–57]. In some cases, a multideposition process can avoid the intermediate pyrolysis step, i.e. only solvent drying is performed. In these cases the problem of liquid movement can be minimized; however, the difficulties encountered to pyrolyze a thick film remain unchanged [20].

In the present study, we report a suitable strategy to avoid liquid movements based on a specific design of a metalorganic low-fluorine ink and an optimized drop on demand deposition protocol. Afterwards, an optimized pyrolysis process, keeping a very good thickness and composition homogeneity is also defined. The validity of this approach is confirmed by X-ray diffraction (XRD) and Scanning Transmission Electron Microscopy (STEM) studies showing that a high quality epitaxial structure is achieved in pristine YBCO and YBCO-$BaZrO_3$ nanocomposite thick films based on a single deposition CSD approach.

To overcome the drawback of liquid movement during deposition and drying we have formulated inks with a low evaporation rate which facilitate droplet merging without coffee ring effects. Pitch of drop on demand deposition in IJP allows to define a precise control of film thickness as well as a very good homogeneity. We have also shown that including a photocurable varnish allows to better pin the liquid through illumination with a UV LED lamp. Then, we use the extensive knowledge previously generated about the physicochemical transformations of the films during the pyrolysis treatment to optimize this step for YBCO thick films (final thickness in excess of 1 µm prepared through a single deposition) [37]. Finally, the epitaxial growth conditions defined previously for CSD based YBCO thick films [31,58] have been used to demonstrate that high critical currents are achieved in IJP pristine and nanocomposite YBCO thick films.

RESULTS AND DISCUSSION

Ink design, drop formation and solution deposition

The first goal of this work is to formulate inks suitable for inkjet-printing (IJP) of thick films while preserving a homogeneous liquid spread during deposition and drying. This requirement is a critical issue in IJP of thick films. It is, therefore, very important to select the solvent and salt concentration and, eventually the use of other chemicals, to control the rheological properties of the inks. The final ink should also be stable and have physical and chemical properties compatible with the printhead. After achieving a suitable ink, the next step is the solution deposition with the appropriate drop density to reach the maximum thickness avoiding any liquid displacement.

There exists a broad expertise in low-fluorine Trifluoroacetate (TFA) solution formulation, adapted to spin coating, which provide clues for designing novel inks adapted to IJP. Several works have demonstrated that IJP can be performed with YBCO CSD inks leading to final film thicknesses in the range of 300-400 nm [20,44,45]. Here our target is to reach a final thickness around 1 µm with a single deposition; this aim requiring a drastic modification of the ink formulation. Eventually, the deposition step can be repeated to further increase the final thickness.

The first strategic decision in the ink design is the solvent selection to tune key properties, such as the evaporation rate. Increasing the solvent boiling point (Table I) allows to reduce solvent evaporation during deposition while keeping similar fluid properties (viscosity, density, surface tension). These parameters need to be combined to have a good droplet jettability with the piezoelectric printhead (Table II). The suitability of a given solution for IJP is determined by the inverse of the Ohnesorge number, Z^{-1} [20,41,45]:

$$Z = Oh^{-1} = \frac{\sqrt{\rho l \gamma}}{\eta} \qquad [1]$$

Table I: Solutions having different boiling points tested to prepare inks for thick film preparation by IJP

Solution	Solvent 1 (%v/v)	b.p. (°C)	Solvent 2 (%v/v)	b.p. (°C)
1	Methanol (74)	64.7	Propionic acid (16)	141.2
2	Propionic acid (100)	141.2	---	---
3	Ethanol (100)	78.2	---	---
4	Butanol (80)	117.7	Propionic acid (20)	141.2

Table II: Ink parameters defining their adaptability to IJP film deposition. Four different solutions were tested with different concentrations and one of them having a varnish (V) as an additive. Oh is the Ohnesorge number and $Z=Oh^{-1}$.

Solution (concentration)	Density ρ (g/ml)	Viscosity η (mPa· s)	Surface tension σ (mN/m)	Contact angle θ (°)	Oh	Z
1 (1.5 M)	1.12	12.0	25.1	33.7	0.29	3.4
1 (0.5 M)	0.89	1.1	22.4	12.5	0.03	32.1
2 (0.5 M)	1.02	1.7	25.4	0.9	0.04	23.6
4 (0.5 M)	0.95	4.1	25.3	5	0.10	9.4
4 (1.0 M)	1.06	9.0	25.4	10	0.17	5.8
4 + V 6,6 $\%_{V/V}$ (1.0 M)	1.07	8.0	25.6	19.7	0.20	5.06

where η is the viscosity, γ the surface tension, ρ the density of the ink and l is the nozzle diameter. In order to have a good droplet formation Z should be at most around 10 [41,45]. Although in our case some of the solutions had higher Z values (Table II), they were still suitable to prepare films by IJP.

Successful control of the film formation by IJP requires to form droplets without satellites and a reproducible volume. For this purpose, drop visualization with stroboscopic cameras is essential. In the Materials and Methods section we describe the typical electronic excitation values used with the piezoelectric head to achieve droplet volumes in the range of 30 -140 pL, while in the S.I. we provide a typical droplet image obtained with the stroboscopic camera, showing that single droplets with diameter ~ 40 μm are formed (Fig S1). Minor adjustments of the piezo waveforms and container pressure were required to achieve stable droplets with the different inks of Table II. The droplet volume and contact angle determine the drop footprint after deposition (see Figure S2). Through modified piezoelectric activation parameters, we could achieve deposited diameters in the 160 – 340 μm range (see typical droplets in Figure 1(a)). Concerning the film thickness, it is determined by the selection of XY pitch of the deposited droplets. In our case, we used a single nozzle deposition system following a line-by-line protocol in a XY movable table (see Methods and Figure S3). First initial tests of IJP film preparation were made with intended final thicknesses in the range of 500 – 1400 nm to analyze the suitability of the different inks. For this purpose, we typically used square-like XY pitches in the range of 25x25 μm, although these values were later further optimized to achieve high quality homogeneous thick films, as it will be described below.

The first tests of IJP film deposition with solutions 1 and 3 immediately showed that they lead to an excessive liquid drag, due to the fast evaporation of the methanol and ethanol solvents which then generated liquid movement driven by capillary forces and so the thickness was very inhomogeneous (Figure S4).

Therefore, we concentrated our ink optimization efforts on solutions 2 and 4 having higher boiling points. In this case, due to a slower evaporation at room temperature, the film remains wet during deposition and so the liquid drag effect is avoided. The main differences between solutions 1 and 4 are the higher viscosity and the reduced contact angle of solution 4 (see Table II). Solutions 2 and 4 with concentrations of 0,5 M lead to an improved liquid distribution after IJP; however, they still display some coffee ring effect and so a more detailed analysis of the deposition process was required. In the case of solution 2, having a relatively low viscosity, we also analyzed the influence of including polymeric additives, such as polyethylene glycol (PEG) which had previously demonstrated to be useful in increasing film thickness by spin coating [59]. We were able to considerably increase the ink viscosity up to the maximum practical limit of the IJP nozzle (~ 20 mPa s), however, huge liquid movements were detected in this case.

For this reason, we performed a more detailed analysis of the droplet volume, the spread of the isolated drops after deposition and the droplet and line merging processes. Our study was performed through a modification of the drop pitch along X when using inks 2 and 4 with 1 M concentration (Table II). Figure 1(a) displays typical isolated droplets with footprint diameters of 162 and 344 μm deposited from inks 4 and 2, respectively. Despite the smaller volume, the drop of ink 2 has a larger footprint than ink 4 due to its lower contact angle (Table II).

Good line merging of the droplets was achieved with a typical X pitch of 50 μm when the droplet volume was 78 and 32 pL, for inks 4 and 2, respectively (Figures 1(b) and 1(c)). In the case of ink 4, a very smooth droplet merging is achieved leading to lines with widths in the range of 250 μm and so this ink was considered to behave very promising. We proceeded then, as a next step, to an analysis of the line merging process by modifying the Y pitch in the range of 1.000 – 50 μm while keeping the X pitch to 50 μm (Figure 2). A different Y pitch was needed in both types of inks to achieve a full liquid covering of the substrate, in accordance with the different drop footprints of inks 2 and 4. In both cases, however, a macroscopic coffee ring is detected by observing a C-shape of the whole liquid in the substrate, thus indicating that the dried lines are still sucking to a certain extent the liquid from the last deposited lines. The main consequence of this thickness inhomogeneity is the formation of cracks originated during pyrolysis in the thickest regions (Figures 3(a) and 3(b)).

When solution 2 is used, a homogeneous liquid distribution is achieved during deposition but the thickness becomes inhomogeneous during drying due to liquid retraction. We conclude, therefore, that ink 4 is the most promising one to develop thick YBCO films by IJP with single deposition, provided that the liquid movement can be avoided.

Owing to the fact that we require to minimize liquid movements after deposition, we modified our inks by including UV photocurable varnishes having the potential to minimize the liquid displacement [60]. After testing several of them, we found that a varnish (V) based on polyacrylic esters can be included in our inks without affecting its stability, keeping a similar viscosity and droplet jettability, but having as a positive asset an increase of the wetting angle (θ =19º, as compared to 5-10º without V for ink 4) (see Table II). The selected varnish V has an optical absorption peak at 382 nm (Figure S5) and so we used a LED lamp of λ = 395 nm to initiate the polymerization triggered by the UV lamp. After the ink deposition a photocuring process was applied to the film with a LED power input of 0.7 W during 5 minutes. The changes of ink properties are reflected in an improved stability of the merged lines with a droplet volume of 65 pL (Figure 4(a)). With ink 4 at 1M including V 6-10 $\%_{V/V}$ we were able

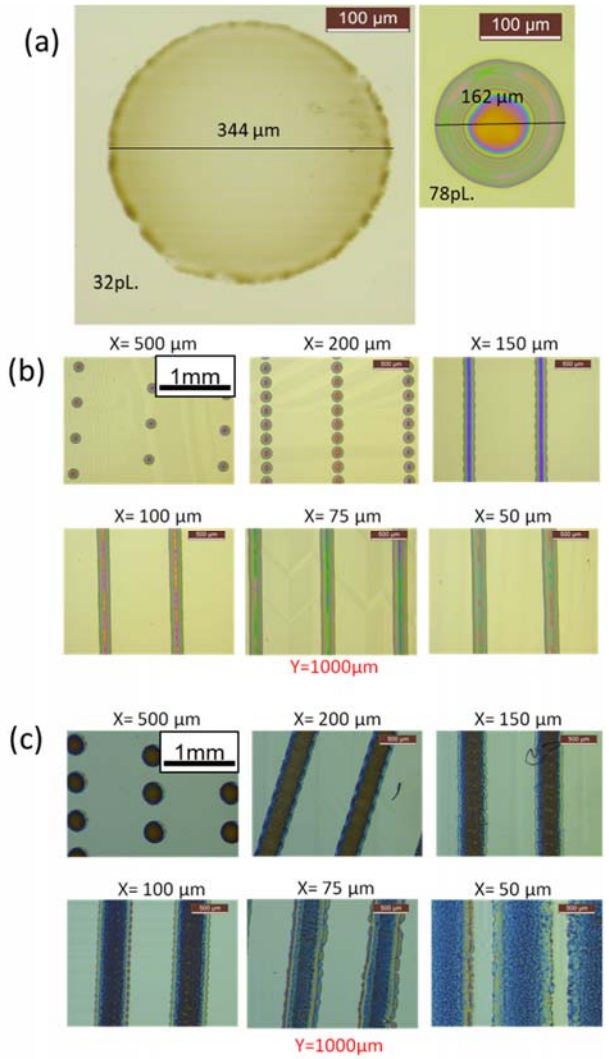

Figure 1.- (a) Typical optical microscopy image of the drop footprints after IJP deposition. In this case the droplets correspond to solution 2 and 4 and they have volumes of 32 pL (diameter of 40 µm) and 78 pL (diameter of 100 µm), respectively. The footprints on the LAO substrate are circles of 344 and 162 µm of diameter, respectively; (b) and (c) Optical microscopy images to study drop merging to form lines. The Y spacing among lines is kept to 1.000 µm in all cases while X spacing is varied, as indicated in the images, from 500 µm to 50 µm. (b) corresponds to ink 4 and (c) corresponds to ink 2, both of them with 1M concentration. The different homogeneity of the merged lines is clearly dependent on the ink properties.

to achieve fairly homogeneous thick films after deposition and drying (Figure 4(b) as compared to Figure 2(a)). We note that some positive influence of including varnish V was also detected with solution 2 but in that case some liquid retraction leads to a severe film inhomogeneity. The final step to optimize the ink deposition relates to the scheduled drop overlap by changing Y pitch. We found that, typically, 35 % overlap of the footprint surface leads to homogeneous films for ink 4+ V 6% $_{V/V}$ (see Figures 4(b) and S6). This optimized selection of drop volume, its footprint and XY pitches in the IJP process allowed, therefore, to achieve a robust deposition with a high thickness homogeneity in the wet and dried stages and so we have been successful in the first step towards the production of films with a final thickness around 1 micron. In conclusion, ink formulation for IJP is a critical issue to develop thick CSD films. First, the solvent selection needs to consider the salt solubility, the fluid conditions which should be compatible with the IJP head and the possibility of drop formation. Second, the wettability of the droplets on the surface needs to be optimized to avoid an excessive spread. Third, the IJP drop deposition conditions need to be defined accordingly with the wettability of the substrate and the evaporation rate of the solvent. And finally, the UV photocuring process allows to keep a homogeneous film thickness after the ink deposition. Our strategy has been to keep wet the film during the whole deposition process while the contact angle is high enough to avoid drop displacement. This issue was favored by including an acrylate-based varnish to the ink which increases the contact angle (see Table II), it hampers the evaporation by weak chemical interactions with the solvent and the existing organic salts and, finally, it fixes the liquid distribution through a polymerization initiated by a photocuring process. After analyzing the drop merging process, the deposition pitches have to be tuned to achieve the desired final film thickness considering the salt concentration in the ink. Performing a wise selection of all these parameters allows achieving homogeneous wet and dried films with expected final thicknesses in the range of 1 micron.

Pyrolysis of thick films

After optimizing the solution composition and deposition process, the next key step requiring a fine tuning in the development of thick CSD films is the pyrolysis process. During pyrolysis all the organic precursors are converted to inorganic nanometric or amorphous precursors (CuO and $Ba_{2-x}Y_xF_{2+y}$ (BYF) in the present case, see the chemical transformations in eq. 1) [4,24,38,61–64].

$$Y(TFA)_3 + 2Ba(prop)_2 + 3Cu(prop)_2 \longrightarrow (1/x)(Ba_{1-x}Y_x)F_{2+x} + 3CuO \quad \text{[Eq. 1]}$$

We note that the requirements of this step are exactly the same when a multideposition approach is followed without intermediate pyrolysis treatments [20]. Understanding the physico-chemical transformations occurring in films during the pyrolysis step is essential to succeed in keeping the films homogeneous. Wrinkling and cracking are the most annoying film instabilities and

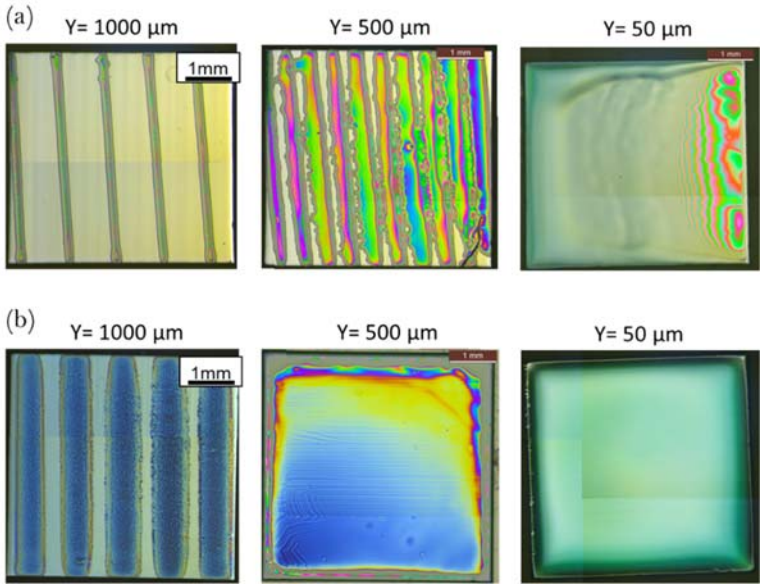

Figure 2.- Optical microscopy images to study the line merging using a constant drop spacing in X direction of 50 µm and varying Y spacing from 1000 µm to 50 µm, as indicated. (a) Images corresponding to ink 4 with 1M concentration; (b) Equivalent optical images of line merging of ink 2 with 1 M concentration. The liquid movement towards the first deposited lines (at the left of the figures) leads to the C-shape of the whole liquid deposited on the substrate. The higher wettability with ink 2 is evidenced by the reduced number of lines required to fully cover the substrate.

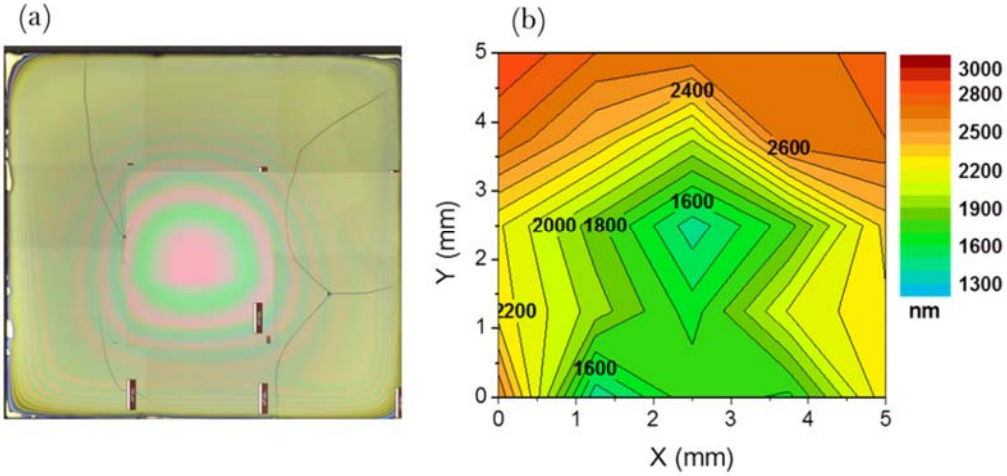

Figure 3.- (a) and (b) A typical optical image and the corresponding thickness map of a pyrolyzed film of solution 4 displaying a strong thickness inhomogeneity. The coffee-ring effect leading to a C-shape liquid distribution is clearly appreciated in the film thickness map. The crack formation originated at the thickest parts of the film is appreciated on the optical image.

they are associated to in plane stresses created by the film volume retraction and the differential film-substrate thermal expansion during the pyrolysis.

In low-fluorine YBCO films (TFA and propionate precursors) three different temperature regions have been identified and widely investigated: zone I (T< 150 ºC) where the film dries, zone II (150-240 ºC) where wrinkling occurs as a reversible or irreversible phenomenon and zone III (240-320 ºC) where cracking may eventually be generated, depending on the heating rate [37,62]. We used, therefore, the existing knowledge about these processes to optimize the heat treatment steps and the varnish content in ink 4+V.

The first parameter to be optimized was the varnish content which was varied in the range 3-10 $\%_{V/V}$. The heating rates were 25 °C/min for zone I and 2 °C/min for zones II and III. Optical interferometry showed that the film thickness after drying (zone I) increases to 17 µm for ink 4+V with 10 $\%_{V/V}$ content, as compared to 7 µm for ink 4. This indicates that the weak chemical-bonding (H bonding and dipolar interactions) of acrylate varnish with the initial metalorganic skeleton (TFA and propionates) strongly modifies it, as it could be expected from the strong ability of acrylates to form polymers [65]. These films having an initial large thickness displayed reversible wrinkling in

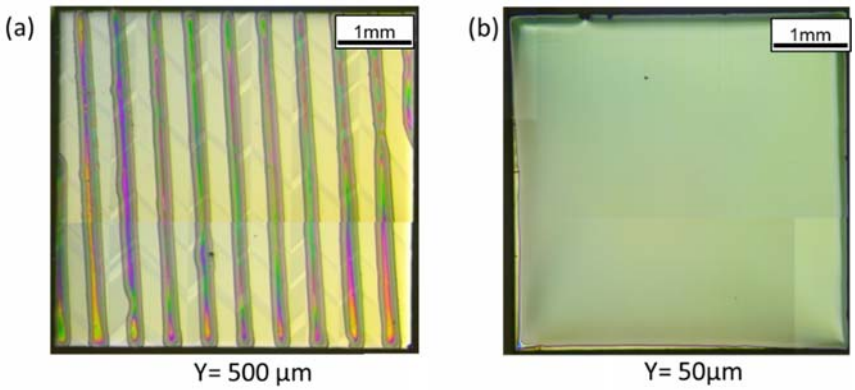

Figure 4.- Optical microscopy images showing: (a) the continuous and sharp lines obtained for ink 4 + V 6,6 %$_{V/V}$ using a constant drop spacing in X direction of 50 µm and (b) the homogeneous film formation with the same ink for an Y spacing of 50 µm.

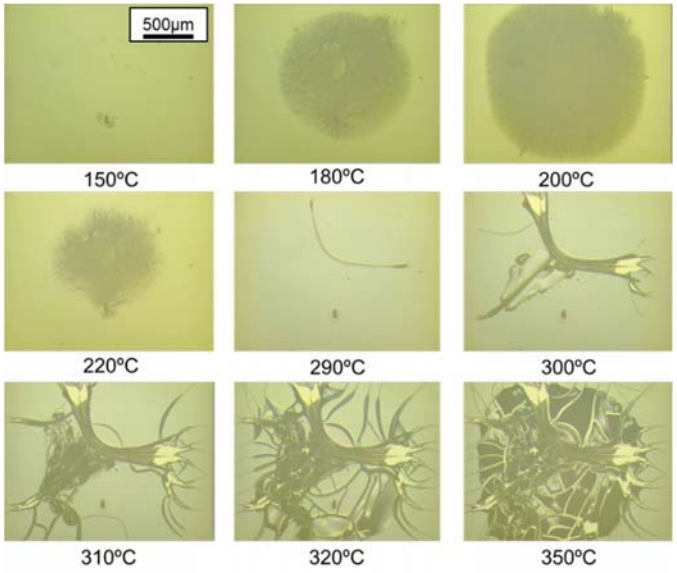

Figure 5.- Optical microscopy images obtained in-situ during the pyrolysis of a film with a nominal final thickness of 700 nm prepared by IJP with ink 4 (1 M)+V 10%$_{V/V}$ with a heating rate of 2° C/min. The corresponding temperature of each image is indicated. Reversible wrinkling is first observed (zone II, 180 – 220° C) and cracking and delamination (zone III, T> 290° C). See also Video S1 in S.I.

zone II and a strong tendency to crack formation, and even delamination, within zone III (see Figure 5 and Video S1 in S.I.). As it has been mentioned previously, film cracking is generated by a strong in-plane tensile stress associated to the film shrinkage when it is attached to the substrate. For a given stress σ, a critical film thickness t_c marks the maximum thickness where cracks are still not formed:

$$t_c = \frac{2G_c E}{Z\sigma^2(1-\nu)} \qquad \text{[Eq. 2]}$$

where G_c is the energy needed to form two crack surfaces, E is Young's modulus, ν is the Poisson's ratio, Z is a dimensionless geometrical parameter and σ is the biaxial tensile stress of the film [1,2,9].

To avoid the detrimental effects of an excessive film shrinkage, we tuned the varnish content to keep, both the positive effect of an enhanced thickness homogeneity during deposition, and an affordable tensile stress during the film shrinkage. We found that a reasonable balance between both competing trends could be achieved with a 6.6 %$_{V/V}$ content of varnish. So this particular composition was thoroughly investigated.

In-situ OM video recording during different heating rates determined the critical heating rate in zone II to keep reversible wrinkling in films prepared with ink 4+V 6.6 %$_{V/V}$. We found that the varnish allows to increase the heating rate in region II to >20 °C/min, with reversible wrinkling, as compared to a maximum of 15 °C/min for ink 4 (Video S2 in S.I.). It was also concluded that under the same heating rate in region III (10 °C/min) the onset of cracking is retarded by the varnish by about 40 °C (300 °C instead of 260 °C) (Video S3 in S.I.). Overall, therefore, we conclude that including the varnish in ink 4, not only has a positive effect on impeding the liquid movement during deposition, it also improves the stability of the film during pyrolysis. To clarify the origin of this remarkable influence, we investigated the decomposition process of the film through the mass evolution, by means of TGA and the volatiles by EGA-FTIR and MS. In parallel, the film thickness evolution was investigated

through in-situ optical interferometry (Figures 6(c) and 6(d)). The comparison of TGA of solution 4+V film with that of solution 4 (Figure 6(a)) reflects a higher organic loss in the 4+V film, due to the additional organic mass of this ink. Through simultaneous TGA/EGA-FTIR (Figures 6(b) and S7) and EGA-MS analyses it was verified that the volatiles including TFAH and most of the propionates were decomposed below ~300 °C, similarly to solution 4 (ref 37), while the last peak in the dTG (Figure 6(b)) and DSC (Figure S7) (T ~309 °C) corresponding to CO_2 very likely is associated to the decomposition of some acrylate derivatives. This result correlates with the higher decomposition temperature of varnish V when it is not linked to the main TFA – propionate metalorganic skeleton (Figure S8). Hence we conclude that there is some coordination of the acrylate and propionate precursors and this is the reason of observing the final decomposition of solution 4 + V 6.6 $\%_{V/V}$ at higher temperatures than solution 4.

Concerning film thickness, we realize that at 150 °C the thickness for the 4+V 6.6 $\%_{V/V}$ ink is about twice that of ink 4 (Figure 6(c), the mass increase was only about 10 % (Figure 6(a)), thus confirming our claim that the metalorganic skeleton was deeply modified by the varnish addition, i.e. it becomes less dense (10 % increase of mass enhances the thickness 100%). On the other hand, when the thickness evolution during heating is normalized (Figure 6(d)), some smoothing of the shrinkage (temperature dependence of thickness) is detected in region III (T> 270 °C) in films with ink 4+V 6.6 $\%_{V/V}$. Since this is precisely the temperature range where cracks develop in these thick films, the observed different thickness evolution is very relevant.

In this high temperature range of region III (T > 270 °C), as we mentioned above, a small fraction of the metalorganic skeleton (mainly acrylate derivatives) remains while the film becomes stiffer when the transformation to a nanoporous solid occurs [37]. Preserving part of the acrylate molecular skeleton at higher temperatures softens the elastic solid associated to the inorganic amorphous or nanocrystalline nanoparticles, thus smoothing the shrinkage process [54].

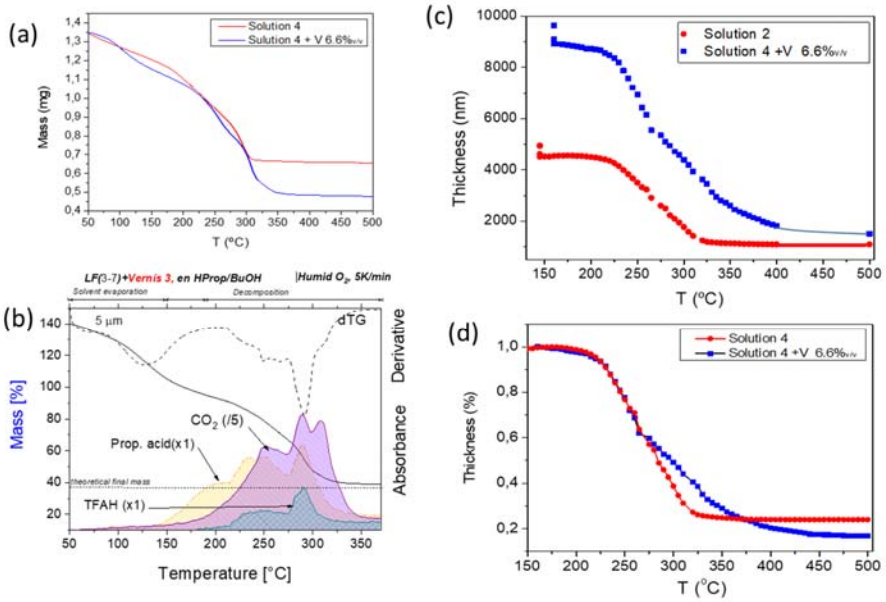

Figure 6.- (a) TGA of the mass loss during pyrolysis for films with a nominal final thickness of 850nm using ink 4 and ink 4 + V 6,6 $\%_{V/V}$; (b) TGA and dTG of ink 4 + V 6,6 $\%_{V/V}$ together with the evolution of the FTIR intensity at selected frequencies corresponding to characteristic CO_2, TFAH and propionic acid absorptions. Note the scale changes; (c) Film thickness evolution with temperature during pyrolysis (heating rate 5 ºC/min) of the two films shown in (a), as determined by in-situ optical interferometry; (d) Curves of figure (c) normalized.

We may wonder why displacing the shrinkage at higher temperatures would improve the resilience of the films against crack formation. Actually, the in-plane tensile stress is created due to the rigid attachment of the film to the substrate. Increasing the temperature where shrinkage is completed enhances atomic diffusion (a thermally activated process) and so the in-plane tensile stress σ is partially relaxed. Owing to the strong dependence of the critical film thickness for crack generation with the tensile stress ($t_c \propto 1/\sigma^2$, eq. 2), some increase of t_c should be expected when σ is decreased, as it is indeed observed when films with different nominal final thicknesses are prepared. Figures 7(a) and 7(b) show OM images and the corresponding thickness map of pyrolyzed films with the largest thickness achieved so far with a single IJP deposition (~ 2.000 nm after pyrolysis) (Figure 7(a)). Figure 7(b) shows a film where cracks start to form in the central part of the film where thickness is larger. We note that these films display a fairly good thickness homogeneity, in the range of 5 %.

As it may be observed in the SEM cross section images of films prepared by FIB (Figure 8), a homogeneous microstructure

across the whole section is achieved in the pyrolyzed films. We also note that a refined porosity is obtained in the films including varnish. Probably this is due to the modified structure of the initial metalorganic skeleton which evolve differently during the pyrolysis process, as reflected in the thickness dependence (Figure 6(c)) and also to the different final temperature of the pyrolysis.

We conclude, therefore, that including an acrylate-based varnish to solution 4 allows, not only to enhance the film thickness homogeneity after IJP deposition and drying, as we described in the previous section, it also improves the resilience of the films against the formation of wrinkles and cracks during the pyrolysis process. Hence, the microstructure of these pyrolyzed films fulfill the requirements for the development of high quality epitaxial YBCO thick films. We should note that all the described processes to prepare IJP YBCO films were also successfully applied, with minor adaption, to buffered metallic substrates such as $^{CSD}CeO_2/^{ABAD}YSZ/SS$ supplied by Bruker HTS [46] and so they are suitable for the preparation of long length coated conductors (Figure S9).

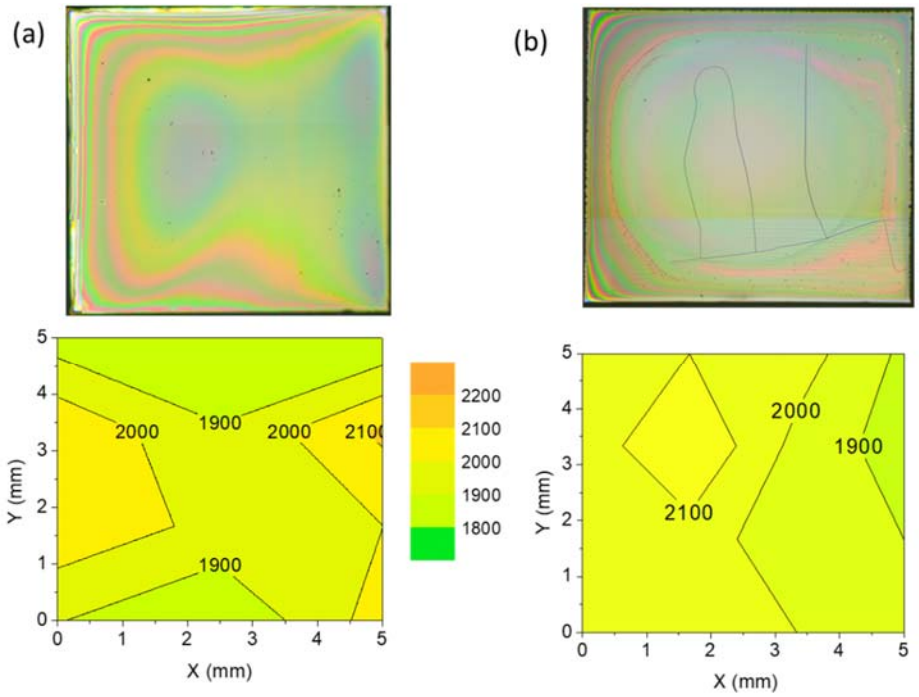

Figure 7.- Optical microscopy images of IJP films (5 x 5 mm) after pyrolysis and the corresponding thickness maps, determined by optical interferometry. The used ink was 4 + V 6,6 $\%_{V/V}$ and the heating rate was 5 °C/min. (a) Homogeneous film with a final nominal thickness of ~ 1.100 nm not displaying any crack; (b) film with a final film thickness of ~ 1.050 nm showing a few cracks in the central part of the film. See also Videos S2 and S3 in S.I.

Growth, microstructure and superconducting properties of homogeneous thick YBCO films

Growth of epitaxial YBCO films following the TFA and the low fluorine CSD route have been widely investigated previously [4,22,33,57,64]. When thick films growth is performed special care is required to control the supersaturation conditions which influence the nucleation and growth processes [31,58]. Several investigations have concluded that to keep a high microstructural homogeneity, and so a high superconducting performance (critical current), separate heating steps for the nucleation and growth steps should be followed [31,34,64]. It was also demonstrated that an improved control of the epitaxial nucleation was achieved by adding small amounts of Ag(TFA) to the ink which decreases the supersaturation strength [31]. Finally, it has been also demonstrated by several authors that high performance epitaxial nanocomposite films can be grown using colloidal metalorganic solutions including pre-prepared nanoparticles, such as $BaMO_3$ (M= Zr, Hf, Ti) perovskites which are not reactive with the YBCO precursors [15,17,18]. We have, therefore, prepared stable colloidal inks including $BaZrO_3$ nanoparticles ready for single deposition IJP of YBCO thick films and we have investigated the corresponding pyrolized process. The objective was to prepare YBCO nanocomposite films with a thickness in the range of 1 μm. Essentially, the ink preparation and the IJP process followed similar procedures than those described in the previous sections for pristine films (see Preparation and methods).

High temperature growth of YBCO was performed following the conventional thermal annealing (CTA) previously described for thick films [2,31,63]. It consists of a heating ramp at 25° C/min in a mixture of wet (P_{H2O}= 200 mbar) N_2 and 200 ppm of O_2 up to the nucleation and growth temperature (~770 °C). Then an isothermal thermal period lasting about 180 min is used to grow the film [63].

To assess the film thickness after growth we used a perfilometer which showed that a thickness of 1.1 μm was achieved (Figure 9(a)). This is actually one of the largest epitaxial CSD-YBCO films grown so far using a single deposition process. Additionally, the development of a robust IJP manufacturing process for

thick films could be based on a combination of individual deposition of thick films and a repeated deposition with intermediate pyrolysis treatments [20,31,32]. Just to demonstrate the feasibility of this approach, we prepared double deposited IJP films with a final thickness of 1.6 µm (see Figure 9(b)). These films keep a high quality epitaxial structure although their superconducting properties still require further optimization.

The superconducting properties of YBCO films prepared by IJP and with varying thickness are reported in Figure 10, where the self-field critical current at 77 K measured by transport measurements (see Experimental section) is represented. The $I_c(H, T)$ values achieved at 77 K (I_c ~ 230 A/cm-w at self-field) are very competitive with those achieved through multideposition CSD and vacuum deposition approaches, thus validating the present IJP process [31,33,66,67]. Also the improvement on the magnetic field dependence (smoothing) of $I_c(H)$ in nanocomposite

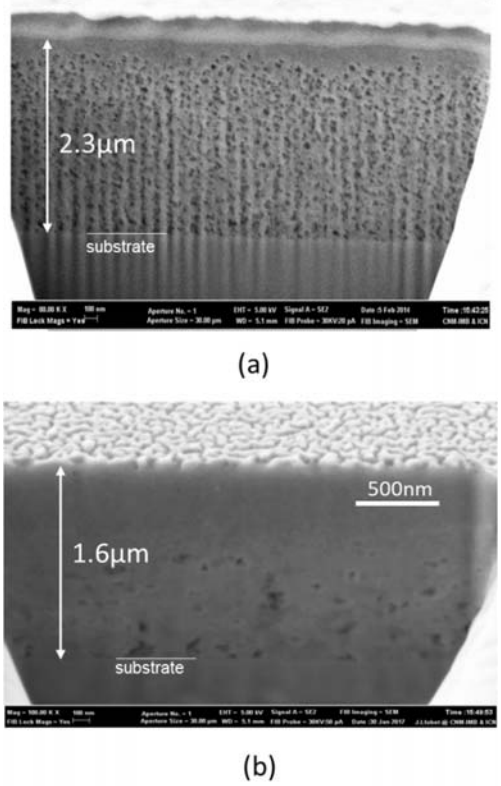

Figure 8.- Scanning Electron Microscopy (SEM) images of $YBa_2Cu_3O_7$ pyrolyzed films' cross section obtained by Focused Ion Beam (FIB). The expected final film thickness was 1 µm. (a) Film prepared with ink 2 and pyrolyzed at 350° C having a thickness 2.3 µm; (b) Film prepared with ink 4 + V 6.6% $_{V/V}$ and pyrolyzed at 500° C having a thickness of 1.6 µm. Note the decrease of porosity in the second film.

thick films (12 % BZO) is visualized in Figure 10(b), where $I_c(H)$ measurements at 77 K of films with different thicknesses and nanoparticle contents are represented. Confirmation of the epitaxial and micro/nano structural quality of the films was achieved from 2D X-ray diffraction patterns, cross section TEM analysis and SEM images (Figures 11(a)-(c) and 12(a)-(c)). In both cases a high quality texture is achieved, as reflected in the GADDS diffraction patterns. Also a fairly small porosity remains as well as a low concentration of secondary phases. The nanocomposite thick films keep a reasonable small nanoparticle coarsening during heating and so the final particle size remains close to the starting one and they induce intergrowths which have a positive contribution to vortex pinning together with the nanoparticles themselves [17].

We conclude, therefore, that the developed IJP approach to YBCO thick films fulfills the strict homogeneity requirements to grow high quality epitaxial thick films and so we envisage that this technique will be further pursued in the future considering its potential for large scale preparation of coated conductors with high critical currents.

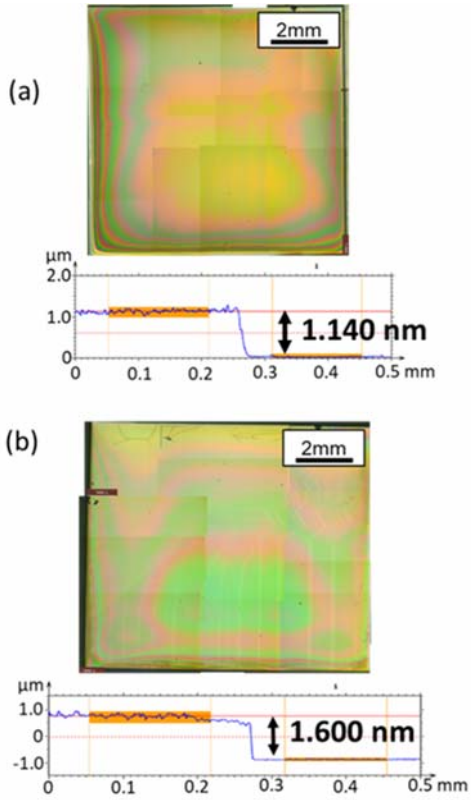

Figure 9.- (a) and (b) Optical microscopy images of IJP $YBa_2Cu_3O_7$ films (10 x 10 mm) after pyrolysis and the corresponding perfilometry scan across an etched part of the $YBa_2Cu_3O_7$ film after growth. Image (a) corresponds to the single deposition with a final film thickness above 1.1 µm. Image (b) corresponds to a film after a second deposition showing that the final film thickness after growth is above 1.6 µm.

CONCLUSIONS

The potential of IJP to prepare micrometric thick YBCO films has been demonstrated. The most suitable physico-chemical properties of the inks to avoid liquid movement, due to coffee ring effect, have been determined. The successful strategy has been to select high boiling temperature solvents (propionic acid and butanol), to minimize solvent evaporation during deposition. Additionally, a low wettability of the substrate to minimize the liquid spread contributes to pin the liquid. This effect has been further enhanced by adding small amounts of a photocurable polyacrylic ester-based varnish to the ink. A UV lamp curing process contributed to pin the liquid after deposition and so

to optimize the thickness homogeneity. Once the ink composition was tested and optimized for IJP, a systematic analysis of the drop on demand deposition protocols were performed to achieve the intended final film thickness, keeping the desired thickness homogeneity. After drying, film thicknesses are in the range of 17 μm for films with a nominal final thickness of 1 μm. Obviously, these films displayed a severe shrinkage during pyrolysis and so the generated in-plane strain may lead to film instabilities, such as wrinkling, cracking or delamination. Appropriate heat treatments were defined, with the support of in-situ-imaging and characterization tools, which allowed to obtain homogeneous films with record values of thickness for a IJP single deposition (~ 2 μm after pyrolysis and ~ 1.1 μm after growth). Further increase of the film thickness was demonstrated using IJP multideposition with intermediate pyrolysis. A significant contribution to increase the critical thickness against crack generation has been associated to the influence of the acrylate precursors of the varnish additive which coordinate with the propionates and the final decomposition occurs at higher temperatures than the propionate and trifluoroacetate salts alone and so an enhanced atomic diffusion contributes to relax the in-plane tensile stress.

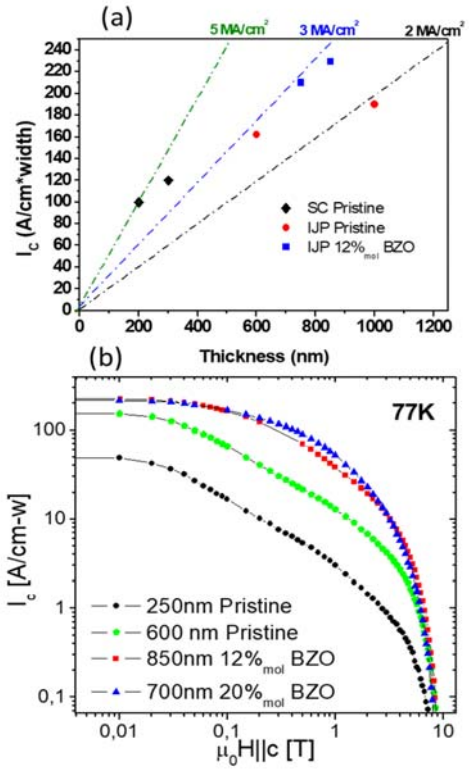

Figure 10.- (a) Critical current I_c per conductor width at self-field and 77 K of $YBa_2Cu_3O_7$ pristine spin coated (SC) and IJP films and $YBa_2Cu_3O_7$+12 $\%_{mol}$ $BaZrO_3$ nanocomposite films prepared by IJP having different film thicknesses. The indicated slopes correspond to the thickness dependence of the critical currents I_c expected for different critical current densities J_c of the films; (b) Magnetic field dependence of the critical current I_c measured at 77 K with H//c in pristine and nanocomposite films with different film thicknesses.

Finally, the homogeneous thick films obtained after pyrolysis have been converted to epitaxial pristine YBCO films through a high temperature crystallization process and the films display high critical currents. The whole process was extended without any essential modification to prepare YBCO – $BaZrO_3$ nanocomposite films derived from colloidal inks including pre-prepared $BaZrO_3$ nanoparticles. In conclusion, our approach suggests that IJP can be properly used as a very attractive tool to prepare functional thick films having maximized performance.

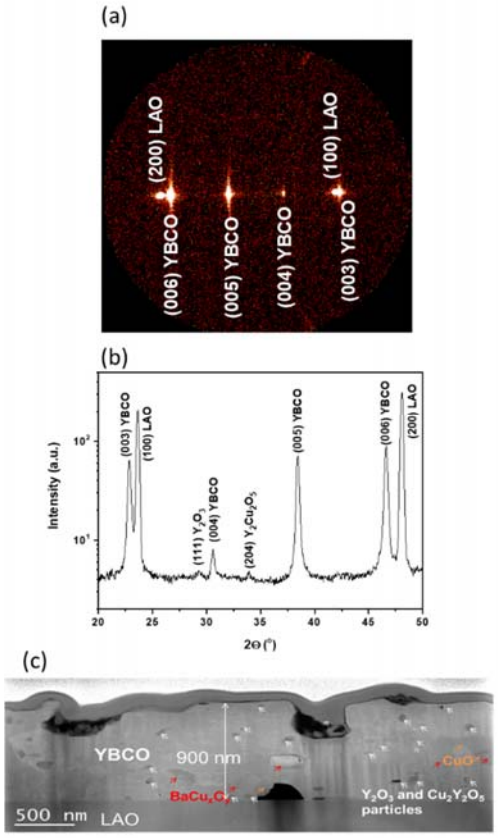

Figure 11.- Typical X-ray diffraction patterns and cross section STEM image of a pristine $YBa_2Cu_3O_7$ film prepared by IJP in a single deposition with a final thickness of ~ 900 nm. (a) GADDS and (b) integrated θ-2θ XRD pattern of the film; (c) Low resolution STEM image of the film showing some residual secondary nanoparticles trapped in the $YBa_2Cu_3O_7$ matrix (Y_2O_3, $Y_2Cu_2O_5$ and $BaCu_3O_x$).

MATERIALS AND METHODS

YBCO Precursor solutions

The YBCO precursor solutions used in this work were prepared through a low-fluorine route based on Ba and Cu acetates (anhydrous $Ba(OAc)_2$ and $Cu(OAc)_2$ Aldrich) and Y trifluoroacetate (anhydrous Y-TFA, Aldrich). The stoichiometric amount (Y:Ba:Cu = 1:2:3) of precursor salts was dissolved in different solvents (methanol, ethanol, propionic acid, butanol), as indicated in Table I, to prepare inks with different rheological properties and concentrations (Table II) and to investigate its suitability for Ink Jet Printing. The precursors were prepared as described before [57] with metal concentrations in the range of 0.5 - 1.5 M (sum of metals). In some cases, solution 3 (ethanol) and

4 (butanol and propionic acid), a polyacrylic ester -based varnish (V), provided by KAO Chimigraf Company (Rubí, Spain), was used as an additive to the inks, with concentrations up to 10 $\%_{V/V}$, to tune their wettability on the oxide substrates (see Table II) and using a photocuring process to fix the liquid in the substrate. The substrates were $LaAlO_3$ (LAO) single crystals but the suitability of oxide buffered metallic substrates, such as ABAD (Alternating Beam Assisted Deposition) SS/YSZ/CZO (SS=stainless steel; YSZ=ZrO_2:Y; CZO= $Ce_{1-x}ZrO_{2-y}$ deposited by CSD; provided by Bruker HTS), was also demonstrated [31,46]. An additional advantage of using the varnish additive V is that Thermogravimetric Analysis (TGA) shows that it completes its decomposition at higher temperatures (see Figure S7 in the S.I.) than the metalorganic salts forming the molecular skeleton of our films

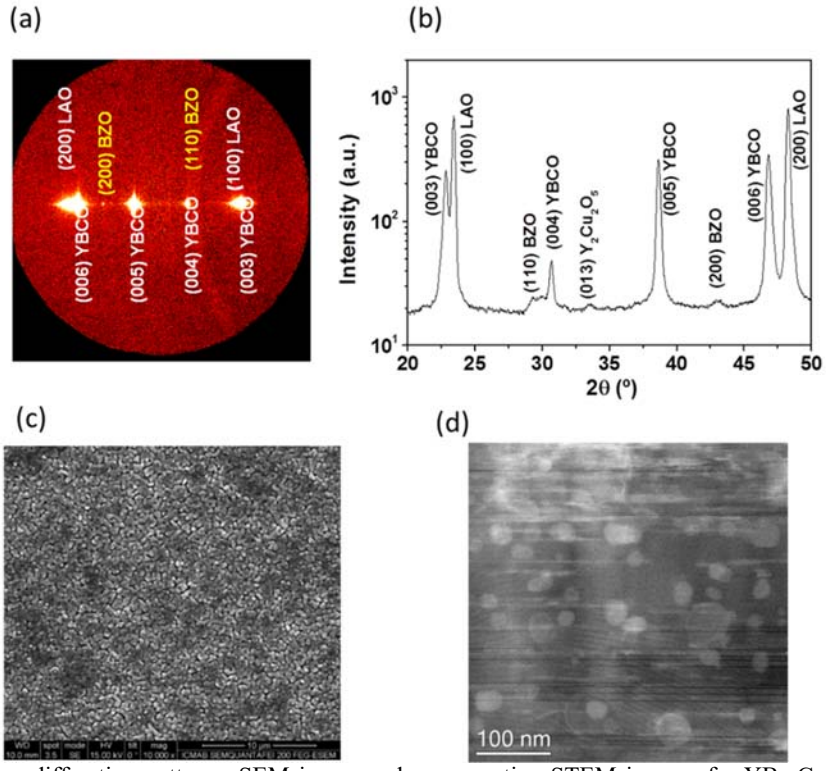

Figure 12.- Typical X-ray diffraction patterns, SEM image and cross section STEM image of a $YBa_2Cu_3O_7$ + 12 $\%_{mol}$ $BaZrO_3$ nanocomposite film with a thickness of 850 nm after growth and a critical current at self-field and 77 K of I_c= 230 A/cm-w. (a) GADDS XRD pattern, and (b) integrated θ-2θ XRD pattern of the film; (c) SEM image of the film surface; (d) High resolution STEM image of the nanocomposite films where the $BaZrO_3$ nanoparticles are visualized.

(TFA and propionates) [37] and so it may also influence the pyrolysis process. An additional additive was used to promote the epitaxial nucleation step (Ag TFA) while nanocomposite superconducting films were prepared to enhance the in-field properties ($BaZrO_3$ nanoparticles) [17,31,68]. Typically, the contents of these additives were 5$\%_{mol}$ Ag(TFA) in the first case and 12% $_{mol}$ $BaZrO_3$ in the second case. The $BaZrO_3$ nanoparticles were synthesized by a solvothermal approach recently described and stabilized in the YBCO precursors[68]. All the YBCO inks prepared display rheological properties suitable for being used to prepare films by IJP (see Table II), they had water contents below 1,5%wt and they were stable for weeks when stored under Ar atmosphere.

Ink Jet Printing system

Ink Jet Printing (IJP) was performed using a single nozzle commercial drop on demand (DoD) piezoelectric (PZT) actuated dispenser (Microfab Technologies, MJ-AB-01-60) with a 60 μm nozzle and pressure control on the ink container. The printhead is stationary during printing (room temperature and controlled dry atmosphere) and a computer-controlled XY table is used to position the substrate following a line-by-line procedure with variable X and Y pitches (micrometer resolution) (Figure S3). The X axis corresponds to the line printing direction and it has a movement speed of 1 cm/s. The droplets are constantly generated at a certain frequency (in the range of hundreds of droplets per second) and so the X pitch can be controlled through any of these two parameters (droplet frequency and table speed). The drop pitch is referred as (X x Y) being X the drop distance in the X axis (μm) and Y the lateral line step used (μm) and so the drop distance along Y axis. The investigated pitches were in the range of 50 – 500 μm for X axis and 50 – 1000 μm for Y axis.

The drops were generated using an asymmetric bipolar squared wave [45]. The waveform is divided in segments which can be individually modified to tune the pulse length and voltage widths to control the droplet volume and frequency. The range of droplet volumes investigated were 30 -75 pL by using pulse lengths in the range of 50 – 60 μs and widths +(20 to 30) V and -(10 to 20) V. Typical values used to form drops were 23 V, -13 V for a pulse length of 53 μs. The drop formation is controlled through a stroboscopic camera (Figure S1 in S.I.) and

the drop volume is calculated using a LABVIEW software and it has a high reproducibility (uncertainty below 10 %).
The films were deposited on 5 × 5 mm^2 (100) commercially available $LaAlO_3$ (LAO) single-crystal substrates which were previously heat treated under oxygen flow at 900 °C during 5 h and on ABAD SS/YSZ metallic substrates from Bruker HTS which were coated by CZO by CSD.

Thermal treatments
After solution deposition, the films follow first a photocuring treatment with a LED lamp (λ=395 nm). After several tests of the UV LED power, we selected an input power of 0.7 W and the curing time was fixed to 5 minutes. Afterwards, two additional thermal treatments were applied. First, the films are pyrolyzed at low temperatures (T< 500 °C) using a process which we have optimized for thick films, based on the knowledge generated in a recent thorough analysis of the physico-chemical transformations of the low-fluorine YBCO CSD films during heating in this temperature range [37]. After pyrolysis, a second high temperature (T< 820 °C) nucleation and growth process of epitaxial YBCO thick films has been carried out [31].
The pyrolysis of the films is performed following a heating process under a humid O_2 atmosphere including three different steps characterized by the heating ramp and the temperature regions. Region I spans from room temperature up to 150 ºC with heating in air under ramps up to 20 ºC/min and a plateau of 45 min. This step allows to dry the film, i.e. the solvent is fully eliminated. Region II spans a temperature window from 150 to 240 °C and the investigated heating ramps were in the range of 1-20 °C/min to assess under which conditions reversible or irreversible wrinkling phenomena occurs in the films. Finally, region III corresponds to the temperature window 240 – 500 °C, the investigated heating ramps were in the range of 5 – 20 °C/min and this region is where cracking may be eventually generate [37]. Within regions II and III the metalorganics progressively decompose and lead to nanometric or amorphous films including the precursors of YBCO, i.e. CuO and $Ba_{2-x}Y_xF_{2+y}$ (BYF). The film thickness evolution during these drying and pyrolysis stages were investigated in-situ through optical interferometry. Typically, after stage I the film thickness is in the range of 10 μm while after region III thicknesses up to 2.000 nm were obtained when a single IJP deposition was performed. After the pyrolysis process, a high temperature annealing is carried out which transforms the inorganic nanometric precursors into epitaxial YBCO films, following a complex intermediate phase evolution, a nucleation step at the substrate interface and a growth process of the whole film. A thorough analysis of these complex processes and the correlation with the processing conditions has been previously described [31,62,63]. Growth of thick YBCO films were performed through a heating ramp of 25 °C/min and annealing at 770 °C during ~180 min. The atmosphere is a mixture of wet (PH_2O=200 mbar) N_2 and O_2 (200 ppm). After growth, the YBCO films are oxygenated at 450 – 550 °C in a dry oxygen atmosphere during 3.5 h. The thickness of the YBCO epitaxial films were determined through perfilometry and the maximum values we could achieve are in the range of ~1100 nm for a single IJP deposition. Double IJP deposition was also carried out with an intermediate pyrolysis process. In that case, homogeneous films with a final thickness of ~1.600 nm could be achieved.

Characterization measurements
Analysis of the metalorganic solutions was carried out by measuring the viscosity with a Haake RheoStress 600 rheometer (ordinary interval around 12-16 mPa·s at 22 °C), the contact angle with a DSA 100 analyzer (ordinary interval around 30°-35° on LAO substrates), the metal stoichiometry was checked by a volumetric assay and this was balanced to the 1:2:3 stoichiometry if necessary by the addition of metal-salts, and the water content in the solutions was measured by the Karl-Fischer method in order to keep it below 1.5 %wt. The $BaZrO_3$ nanoparticle size was determined by light scattering (DLS) using a Zetasizer Nano[68].
Simultaneous Thermogravimetric analysis (TGA) and differential thermal analysis (DTA) were performed in a Mettler Toledo thermo-balance, model TGA/DSC1, at 5 and 20 °C/min under a gas flow of 100 ml/min of a mixture of high purity humid O_2 and synthetic air (Praxair, ≥99.999%). Monitoring of the in-situ generated volatiles were made through in-situ evolved gas analysis (EGA) coupling the TG furnace to a Fourier-transform infrared (FTIR) gas analyzer from Bruker (model ALPHA). Mass spectroscopy MS was performed with a quadrupole (Micro Vision Plus) from MKS. EGA-MS was performed in films placed inside a quartz tube kept at a total pressure around 10^{-5} mbar and heated at a constant rate of 5ºC/min.
Optical microscopy images were recorded with an optical Olympus BX51 microscope coupled to a small heating stage (pyrolyzer), allowing to record in-situ videos during the pyrolysis process. The pyrolizer could control the gas flow and temperature, and heating ramps up to 50 °C/min.
Film thickness measurements of the dried and pyrolyzed films were carried out by optical interferometry (OI) using an apparatus from Filmetrics, model F20-UV with a spot size in the range of 0.7-1.0 μm. In-situ evolution of the film thickness could be determined when the OI was coupled to the pyrolyzer while thickness homogeneity maps could be obtained using an XY displacement stage. Film thicknesses in the range of 20nm to 40μm can be measured using a wavelength range from 190 to 1100 nm. Film thickness of YBCO grown films were determined with a perfilometer P16 from KLA Tencor.
X-ray diffraction of the pyrolyzed and crystallized YBCO films was performed using a Bruker AXS GADDS diffractometer equipped with a 2D detector and operating with Cu Kα radiation. The surface morphology of the YBCO films was investigated using a scanning electron microscopy (SEM, FEI Quanta 200 FEG) and the FIB cross section images were performed by using a dual beam (SEM, FIB) Zeiss 1560 XB apparatus. Scanning Transmission Electron Microscopy (STEM, FEI Titan 60-300 Microscope) was used to record cross section images of the YBCO films after growth. The superconducting properties were measured first inductively using a SQUID magnetometer equipped with a 7 T superconducting coil (Quantum Design, San Diego, CA) and then through electrical transport measurements. Transport critical current measurements were performed in a PPMS Quantum Design system equipped with a 9 T magnet. Narrow bridges of 200 μm lengths and 10 to 30 μm width were fabricated with standard photolithography (Durham Magneto Optics Std MicroWriter). Silver metal contacts were prepared by evaporation and post annealing. I(V) curves curves were measured in a four-point configuration. J_c values were determined following a 10 μV cm^{-1} criterion.

ASSOCIATED CONTENT

Supporting Information description

The Supporting Information is available free of charge on the ACS Publications website.

Additional supporting figures.

The S.I. file includes additional figures to complement those of the main text.

Video S1: Optical microscopy of a film prepared with solution 4 (1 M)+ V 10 %$_{v/v}$ having a final intended thickness of 700 nm and heated from room temperature to 320 ºC at a heating rate of 10°C/min. The film displays reversible wrinkling, crack generation and delamination.

Video S2: Optical microscopy of two films prepared with solution 4 (1M)+ V 6 %$_{v/v}$ having a final intended thickness of 600 and 800 nm and heated from room temperature to 320 ºC at a heating rate of 20 °C/min. The films display reversible wrinkling in region II and no crack generation in region III.

Video S3: Optical microscopy of a film prepared with solution 4 (1M)+ V 6 % $_{v/v}$ having a final intended thickness of 700 nm and heated from room temperature to 320 ºC at 10 °C/min. The film displays reversible wrinkling in region II and crack generation in region III.

AUTHOR INFORMATION

Corresponding authors

* E-mail: **xavier.obradors@icmab.es**

* E-mail: **teresa.puig@icmab.es**

ORCID

Xavier Obradors: 0000-0003-4592-7718

Authors contribution

X.O. and T.P. conceived and designed the experiments. B.V. and F.P. performed the IJP experiments, B.V. and C.P. performed the growth experiments, S.R. designed the ink precursors, X.G. contributed to design the IJP process, A.P., P.R-G., F.V., B.M. and J.F. contributed to the characterization of the films. The manuscript has been written by X.O. with contributions from all the authors. All the authors have given approval to the final version of the manuscript.

ACKNOWLEDGEMENTS

Authors acknowledge the EUROTAPES project (EU-FP7 NMP-LA-2012-280432), COACHSUPENERGY (MAT2014-51778-C2-1-R and MAT2014-51778-C2-2-R) and SUPERINKS (RTC-2015-3840-S) from MINECO (co-financed by the European Regional Development Fund), 2017-SGR 753 from Generalitat de Catalunya, COST Action NANOCOHYBRI (CA16218). ICMAB authors acknowledge the Center of Excellence award Severo Ochoa SEV-2015-0496. Authors acknowledge the Scientific Services at ICMAB, ICN2 Electron Microscopy Division and Dr. B. Mundet for support in growth and TEM of YBCO films.

REFERENCES

(1) Lange, F. F. Chemical Solution Routes to Single-Crystal Thin Films. *Science (80-.).* **1996**, *273* (5277), 903–909.

(2) Schwartz, R. W.; Schneller, T.; Waser, R. Chemical Solution Deposition of Electronic Oxide Films. *Comptes Rendus Chim.* **2004**, *7* (5), 433–461.

(3) Bassiri-Gharb, N.; Bastani, Y.; Bernal, A. Chemical Solution Growth of Ferroelectric Oxide Thin Films and Nanostructures. *Chem. Soc. Rev.* **2014**, *43* (7), 2125–2140.

(4) Obradors, X.; Puig, T.; Ricart, S.; Coll, M.; Gazquez, J.; Palau, A.; Granados, X. Growth, Nanostructure and Vortex Pinning in Superconducting YBa2Cu3O7 Thin Films Based on Trifluoroacetate Solutions. *Supercond. Sci. Technol.* **2012**, *25* (12), 123001.

(5) Briseno, A. L.; Mannsfeld, S. C. B.; Ling, M. M.; Liu, S.; Tseng, R. J.; Reese, C.; Roberts, M. E.; Yang, Y.; Wudl, F.; Bao, Z. Patterning Organic Single-Crystal Transistor Arrays. *Nature* **2006**, *444* (7121), 913–917.

(6) Schultz, C.; Fenske, M.; Dagar, J.; Zeiser, A.; Bartelt, A.; Schlatmann, R.; Unger, E.; Stegemann, B. Ablation Mechanisms of Nanosecond and Picosecond Laser Scribing for Metal Halide Perovskite Module Interconnection – An Experimental and Numerical Analysis. *Sol. Energy* **2020**, *198* (January), 410–418.

(7) Gilshtein, E.; Bolat, S.; Sevilla, G. T.; Cabas-Vidani, A.; Clemens, F.; Graule, T.; Tiwari, A. N.; Romanyuk, Y. E. Inkjet-Printed Conductive ITO Patterns for Transparent Security Systems. *Adv. Mater. Technol.* **2020**, *5* (9), 2000369.

(8) Schneller, T.; Waser, R.; Kosec, M.; Payne, D. *Chemical Solution Deposition of Functional Oxide Thin Films*; Springer, 2013.

(9) Brinker, C. J.; Scherer, G. W. *Sol-Gel Science: The Physics and Chemistry of Sol-Gel Processing*; Academic press, 1990.

(10) Danks, A. E.; Hall, S. R.; Schnepp, Z. The Evolution of 'Sol-Gel' Chemistry as a Technique for Materials Synthesis. *Mater. Horizons* **2016**, *3* (2), 91–112.

(11) Miura, M.; Maiorov, B.; Sato, M.; Kanai, M.; Kato, T.; Kato, T.; Izumi, T.; Awaji, S.; Mele, P.; Kiuchi, M.; others. Tuning Nanoparticle Size for Enhanced Functionality in Perovskite Thin Films Deposited by Metal Organic Deposition. *NPG Asia Mater.* **2017**, *9* (11), e447--e447.

(12) Gutierrez, J.; Llordes, A.; Gazquez, J.; Gibert, M.; Roma, N.; Ricart, S.; Pomar, A.; Sandiumenge, F.; Mestres, N.; Puig, T.; others. Strong Isotropic Flux Pinning in Solution-Derived YBa2Cu3O7-x Nanocomposite Superconductor Films. *Nat. Mater.* **2007**, *6* (5), 367.

(13) Llordes, A.; Palau, A.; Gázquez, J.; Coll, M.; Vlad, R.; Pomar, A.; Arbiol, J.; Guzman, R.; Ye, S.; Rouco, V.; others. Nanoscale Strain-Induced Pair Suppression as a Vortex-Pinning Mechanism in High-Temperature Superconductors. *Nat. Mater.* **2012**, *11* (4), 329–336.

(14) De Keukeleere, K.; Cayado, P.; Meledin, A.;

Vallès, F.; De Roo, J.; Rijckaert, H.; Pollefeyt, G.; Bruneel, E.; Palau, A.; Coll, M.; others. Superconducting YBa2Cu3O7-δ Nanocomposites Using Preformed ZrO2 Nanocrystals: Growth Mechanisms and Vortex Pinning Properties. *Adv. Electron. Mater.* **2016**, *2* (10), 1600161.

(15) Cayado, P.; De Keukeleere, K.; Garzón, A.; Perez-Mirabet, L.; Meledin, A.; De Roo, J.; Vallés, F.; Mundet, B.; Rijckaert, H.; Pollefeyt, G.; others. Epitaxial YBa2Cu3O7-x Nanocomposite Thin Films from Colloidal Solutions. *Supercond. Sci. Technol.* **2015**, *28* (12), 124007.

(16) Obradors, X.; Puig, T.; Li, Z.; Pop, C.; Mundet, B.; Chamorro, N.; Vallés, F.; Coll, M.; Ricart, S.; Vallejo, B.; others. Epitaxial YBa2Cu3O7- x Nanocomposite Films and Coated Conductors from BaMO3 (M= Zr, Hf) Colloidal Solutions. *Supercond. Sci. Technol.* **2018**, *31* (4), 44001.

(17) Li, Z.; Coll, M.; Mundet, B.; Chamorro, N.; Vallès, F.; Palau, A.; Gazquez, J.; Ricart, S.; Puig, T.; Obradors, X. Control of Nanostructure and Pinning Properties in Solution Deposited YBa2Cu3O7-x Nanocomposites with Preformed Perovskite Nanoparticles. *Sci. Rep.* **2019**, *9* (1), 1–14.

(18) Díez-Sierra, J.; López-Domínguez, P.; Rijckaert, H.; Rikel, M.; Hänisch, J.; Khan, M. Z.; Falter, M.; Bennewitz, J.; Huhtinen, H.; Schäfer, S.; others. High Critical Current Density and Enhanced Pinning in Superconducting Films of YBa2Cu3O7-δ Nanocomposites with Embedded BaZrO3, BaHfO3, BaTiO3, and SrZrO3 Nanocrystals. *ACS Appl. Nano Mater.* **2020**, *3* (6), 5542–5553.

(19) Rijckaert, H.; Pollefeyt, G.; Sieger, M.; Hänisch, J.; Bennewitz, J.; De Keukeleere, K.; De Roo, J.; Hühne, R.; Bäcker, M.; Paturi, P.; others. Optimizing Nanocomposites through Nanocrystal Surface Chemistry: Superconducting YBa2Cu3O7 Thin Films via Low-Fluorine Metal Organic Deposition and Preformed Metal Oxide Nanocrystals. *Chem. Mater.* **2017**, *29* (14), 6104–6113.

(20) Rijckaert, H.; Cayado, P.; Nast, R.; Diez Sierra, J.; Erbe, M.; López Dominguez, P.; Hänisch, J.; De Buysser, K.; Holzapfel, B.; Van Driessche, I. Superconducting HfO2-YBa2Cu3O7-δ Nanocomposite Films Deposited Using Ink-Jet Printing of Colloidal Solutions. *Coatings* **2020**, *10* (1), 17.

(21) Soler, L.; Jareño, J.; Banchewski, J.; Rasi, S.; Chamorro, N.; Guzman, R.; Yáñez, R.; Mocuta, C.; Ricart, S.; Farjas, J.; others. Ultrafast Transient Liquid Assisted Growth of High Current Density Superconducting Films. *Nat. Commun.* **2020**, *11* (1), 1–8.

(22) Erbe, M.; Cayado, P.; Freitag, W.; Ackermann, K.; Langer, M.; Meledin, A.; Hänisch, J.; Holzapfel, B. Comparative Study of CSD-Grown REBCO Films with Different Rare Earth Elements: Processing Windows and T C. *Supercond. Sci. Technol.* **2020**, *33*, 094002.

(23) Araki, T.; Hirabayashi, I. Review of a Chemical Approach to YBa2Cu3O7-x -Coated Superconductors—Metalorganic Deposition Using Trifluoroacetates. *Supercond. Sci. Technol.* **2003**, *16* (11), R71.

(24) Holesinger, T. G.; Civale, L.; Maiorov, B.; Feldmann, D. M.; Coulter, J. Y.; Miller, D. J.; Maroni, V. A.; Chen, Z.; Larbalestier, D. C.; Feenstra, R.; Li, X.; Huang, Y.; Kodenkandath, T.; Zhang, W.; Rupich, M. W.; Malozemoff, A. P.; others. Progress in Nanoengineered Microstructures for Tunable High-Current, High-Temperature Superconducting Wires. *Adv. Mater.* **2008**, *20* (3), 391–407.

(25) Queraltó, A.; de la Mata, M.; Arbiol, J.; Obradors, X.; Puig, T. Disentangling Epitaxial Growth Mechanisms of Solution Derived Functional Oxide Thin Films. *Adv. Mater. Interfaces* **2016**, *3* (18), 1600392.

(26) Obradors, X.; Puig, T.; Gibert, M.; Queralto, A.; Zabaleta, J.; Mestres, N. Chemical Solution Route to Self-Assembled Epitaxial Oxide Nanostructures. *Chem. Soc. Rev.* **2014**, *43* (7), 2200–2225.

(27) Larbalestier, D.; Gurevich, A.; Feldmann, D. M.; Polyanskii, A. High-Tc Superconducting Materials for Electric Power Applications. *Nature* **2001**, *414*, 368–377.

(28) Shiohara, Y.; Taneda, T.; Yoshizumi, M. Overview of Materials and Power Applications of Coated Conductors Project. *Jpn. J. Appl. Phys.* **2011**, *51* (1R), 10007.

(29) Obradors, X.; Puig, T. Coated Conductors for Power Applications: Materials Challenges. *Supercond. Sci. Technol.* **2014**, *27* (4), 44003.

(30) Malozemoff, A. P. Second-Generation High-Temperature Superconductor Wires for the Electric Power Grid. *Annu. Rev. Mater. Res.* **2012**, *42*, 373–397.

(31) Pop, C.; Villarejo, B.; Pino, F.; Mundet, B.; Ricart, S.; de Palau, M.; Puig, T.; Obradors, X. Growth of All-Chemical High Critical Current YBa2Cu3O7-δ Thick Films and Coated Conductors. *Supercond. Sci. Technol.* **2019**, *32* (1), 15004.

(32) Nakaoka, K.; Yoshida, R.; Kimura, K.; Kato, T.; Usui, Y.; Izumi, T.; Shiohara, Y. Another Approach for Controlling Size and Distribution of Nanoparticles in Coated Conductors Fabricated by the TFA-MOD Method. *Supercond. Sci. Technol.* **2017**, *30* (5), 55008.

(33) Izumi, T.; Nakaoka, K. Control of Artificial Pinning Centers in REBCO Coated Conductors Derived from the Trifluoroacetate Metal-Organic Deposition Process. *Supercond. Sci. Technol.* **2018**,

31 (3), 34008.

(34) Feenstra, R.; List, F. A.; Li, X.; Rupich, M. W.; Miller, D. J.; Maroni, V. A.; Zhang, Y.; Thompson, J. R.; Christen, D. K. A Modular Ex Situ Conversion Process for Thick MOD-Fluoride REBCO Precursors. *IEEE Trans. Appl. Supercond.* **2009**, *19* (3), 3131–3135.

(35) Llordes, A.; Zalamova, K.; Ricart, S.; Palau, A.; Pomar, A.; Puig, T.; Hardy, A.; Van Bael, M. K.; Obradors, X. Evolution of Metal-Trifluoroacetate Precursors in the Thermal Decomposition toward High-Performance YBa2Cu3O7 Superconducting Films. *Chem. Mater.* **2010**, *22* (5), 1686–1694.

(36) Zalamova, K.; Romà, N.; Pomar, A.; Morlens, S.; Puig, T.; Gázquez, J.; Carrillo, A. E.; Sandiumenge, F.; Ricart, S.; Mestres, N.; others. Smooth Stress Relief of Trifluoroacetate Metal-Organic Solutions for YBa2Cu3O7 Film Growth. *Chem. Mater.* **2006**, *18* (25), 5897–5906.

(37) Villarejo, B.; Pop, C.; Ricart, S.; Mundet, B.; Palau, A.; Roura-Grabulosa, P.; Farjas, J.; Puig, T.; Obradors, X. Pyrolysis Study of Solution-Derived Superconducting YBa2Cu3O7 Films: Disentangling the Physico-Chemical Transformations. *J. Mater. Chem. C* **2020**, *8* (30), 10266–10282.

(38) Armenio, A. A.; Augieri, A.; Ciontea, L.; Contini, G.; Davoli, I.; Di Giovannantonio, M.; Galluzzi, V.; Mancini, A.; Rufoloni, A.; Petrisor, T.; others. Structural and Chemical Evolution of Propionate Based Metal-Organic Precursors for Superconducting YBa2Cu3O7-δ Epitaxial Film Growth. *Supercond. Sci. Technol.* **2011**, *24* (11), 115008.

(39) Dawley, J. T.; Clem, P. G.; Siegal, M. P.; Tallant, D. R.; Overmyer, D. L. Improving Sol-Gel YBa2Cu3O7-δ Film Morphology Using High-Boiling-Point Solvents. *J. Mater. Res.* **2002**, *17* (8), 1900–1903.

(40) Rasi, S.; Soler, L.; Jareño, J.; Banchewski, J.; Guzman, R.; Mocuta, C.; Kreuzer, M.; Ricart, S.; Roura-Grabulosa, P.; Farjas, J.; others. Relevance of the Formation of Intermediate Non-Equilibrium Phases in YBa2Cu3O7-x Film Growth by Transient Liquid-Assisted Growth. *J. Phys. Chem. C* **2020**, *124* (28), 15574–15584.

(41) Derby, B. Inkjet Printing of Functional and Structural Materials: Fluid Property Requirements, Feature Stability, and Resolution. *Annu. Rev. Mater. Res.* **2010**, *40*, 395–414.

(42) Jo, J.-W.; Kang, S.-H.; Heo, J. S.; Kim, Y.-H.; Park, S. K. Flexible Metal Oxide Semiconductor Devices Made by Solution Methods. *Chem. Eur. J.* **2020**, *26*, 9126.

(43) Fortunato, E.; Barquinha, P.; Martins, R. Oxide Semiconductor Thin-Film Transistors: A Review of Recent Advances. *Adv. Mater.* **2012**, *24* (22), 2945–2986.

(44) Van Driessche, I.; Feys, J.; Hopkins, S. C.; Lommens, P.; Granados, X.; Glowacki, B. A.; Ricart, S.; Holzapfel, B.; Vilardell, M.; Kirchner, A.; others. Chemical Solution Deposition Using Ink-Jet Printing for YBCO Coated Conductors. *Supercond. Sci. Technol.* **2012**, *25* (6), 65017.

(45) Vilardell, M.; Granados, X.; Ricart, S.; Van Driessche, I.; Palau, A.; Puig, T.; Obradors, X. Flexible Manufacturing of Functional Ceramic Coatings by Inkjet Printing. *Thin Solid Films* **2013**, *548*, 489–497.

(46) Bartolomé, E.; Vlad, V. R.; Calleja, A.; Aklalouch, M.; Guzmán, R.; Arbiol, J.; Granados, X.; Palau, A.; Obradors, X.; Puig, T.; others. Magnetic and Structural Characterization of Inkjet-Printed TFA YBa2Cu3O7-x/^{MOD}CZO/^{ABAD}YSZ/SS Coated Conductors. *Supercond. Sci. Technol.* **2013**, *26* (12), 125004.

(47) Soltman, D.; Subramanian, V. Inkjet-Printed Line Morphologies and Temperature Control of the Coffee Ring Effect. *Langmuir* **2008**, *24* (5), 2224–2231.

(48) Yunker, P. J.; Still, T.; Lohr, M. A.; Yodh, A. G. Suppression of the Coffee-Ring Effect by Shape-Dependent Capillary Interactions. *Nature* **2011**, *476* (7360), 308–311.

(49) Cobas, R.; Muñoz-Pérez, S.; Cadogan, S.; Ridgway, M. C.; Obradors, X. Surface Charge Reversal Method for High-Resolution Inkjet Printing of Functional Water-Based Inks. *Adv. Funct. Mater.* **2015**, *25* (5), 768–775.

(50) Uchiyama, H.; Shimaoka, D.; Kozuka, H. Spontaneous Pattern Formation Based on the Coffee-Ring Effect for Organic-Inorganic Hybrid Films Prepared by Dip-Coating: Effects of Temperature during Deposition. *Soft Matter* **2012**, *8* (44), 11318–11322.

(51) Ohno, K.; Uchiyama, H.; Kozuka, H. Understanding of the Development of In-Plane Residual Stress in Sol-Gel-Derived Metal Oxide Thin Films. *J. Appl. Phys.* **2012**, *111* (1), 14901.

(52) Kozuka, H. Stress Evolution on Gel-to-Ceramic Thin Film Conversion. *J. sol-gel Sci. Technol.* **2006**, *40* (2–3), 287–297.

(53) Kappert, E. J.; Pavlenko, D.; Malzbender, J.; Nijmeijer, A.; Benes, N. E.; Tsai, P. A. Formation and Prevention of Fractures in Sol-Gel-Derived Thin Films. *Soft Matter* **2015**, *11* (5), 882–888.

(54) Chen, Z.; Burtovyy, R.; Kornev, K.; Luzinov, I.; Xu, D.; Peng, F. The Effect of Polymer Additives on the Critical Thicknesses of Mullite Thin Films Obtained from the Monophasic Sol-Gel Precursors. *J. Sol-Gel Sci. Technol.* **2016**, *80* (2), 285–296.

(55) Kwon, S. J.; Park, J.-H.; Park, J.-G. Wrinkling of a

Sol-Gel-Derived Thin Film. *Phys. Rev. E* **2005**, *71* (1), 11604.

(56) Cop, P.; Kitano, S.; Niinuma, K.; Smarsly, B. M.; Kozuka, H. In-Plane Stress Development in Mesoporous Thin Films. *Nanoscale* **2018**, *10* (15), 7002–7015.

(57) Palmer, X.; Pop, C.; Eloussifi, H.; Villarejo, B.; Roura, P.; Farjas, J.; Calleja, A.; Palau, A.; Obradors, X.; Puig, T.; others. Solution Design for Low-Fluorine Trifluoroacetate Route to YBa2Cu3O7 Films. *Supercond. Sci. Technol.* **2016**, *29* (2), 24002.

(58) Solovyov, V. F.; Li, Q.; Wiesmann, H.; Oleynikov, P.; Zhu, Y. Strong Influence of the YBa2Cu3O7 Grain Size on Critical Current Densities of Thick YBa2Cu3O7 Layers Made by a Metal-Organic Deposition Process. *Supercond. Sci. Technol.* **2008**, *21* (12), 125013.

(59) Morlens, S.; Roma, N.; Ricart, S.; Pomar, A.; Puig, T.; Obradors, X. Thickness Control of Solution Deposited YBCO Superconducting Films by Use of Organic Polymeric Additives. *J. Mater. Res.* **2007**, *22* (8), 2330–2338.

(60) Mendes-Felipe, C.; Oliveira, J.; Etxebarria, I.; Vilas-Vilela, J. L.; Lanceros-Mendez, S. State-of-the-Art and Future Challenges of UV Curable Polymer-Based Smart Materials for Printing Technologies. *Adv. Mater. Technol.* **2019**, *4* (3), 1800618.

(61) Obradors, X.; Puig, T.; Pomar, A.; Sandiumenge, F.; Mestres, N.; Coll, M.; Cavallaro, A.; Roma, N.; Gazquez, J.; Gonzalez, J. C.; others. Progress towards All-Chemical Superconducting YBa2Cu3O7 -Coated Conductors. *Supercond. Sci. Technol.* **2006**, *19* (3), S13.

(62) Zalamova, K.; Pomar, A.; Palau, A.; Puig, T.; Obradors, X. Intermediate Phase Evolution in YBCO Thin Films Grown by the TFA Process. *Supercond. Sci. Technol.* **2009**, *23* (1), 14012.

(63) Li, Z.; Coll, M.; Mundet, B.; Palau, A.; Puig, T.; Obradors, X. Accelerated Growth by Flash Heating of High Critical Current Trifluoroacetate Solution Derived Epitaxial Superconducting YBa2Cu3O7 Films. *J. Mater. Chem. C* **2019**, *7* (16), 4748–4759.

(64) Solovyov, V.; Dimitrov, I. K.; Li, Q. Growth of Thick YBa2Cu3O7 Layers via a Barium Fluoride Process. *Supercond. Sci. Technol.* **2012**, *26* (1), 13001.

(65) Stickler, M.; Rhein, T. Polymethacrylates. In *Ullmann's encyclopedia of industrial chemistry*; Wiley Online Library, 2000.

(66) Feenstra, R.; Gapud, A. A.; List, F. A.; Specht, E. D.; Christen, D. K.; Holesinger, T. G.; Feldmann, D. M. Critical Currents I_c(77 K)> 350 A/cm-width Achieved in Ex Situ YBCO Coated Conductors Using a Faster Conversion Process. *IEEE Trans. Appl. Supercond.* **2005**, *15* (2), 2803–2807.

(67) Majkic, G.; Pratap, R.; Xu, A.; Galstyan, E.; Higley, H. C.; Prestemon, S. O.; Wang, X.; Abraimov, D.; Jaroszynski, J.; Selvamanickam, V. Engineering Current Density over 5 KAmm-2 at 4.2 K, 14 T in Thick Film REBCO Tapes. *Supercond. Sci. Technol.* **2018**, *31* (10), 10LT01.

(68) Chamorro, N.; Martínez-Esaín, J.; Puig, T.; Obradors, X.; Ros, J.; Yáñez, R.; Ricart, S. Hybrid Approach to Obtain High-Quality BaMO3 Perovskite Nanocrystals. *RSC Adv.* **2020**, *10* (48), 28872–28878.

Graphical abstract